

## How merger-driven gas motions in galaxy clusters can turn AGN bubbles into radio relics

JOHN A. ZUHONE,<sup>1</sup> MAXIM MARKEVITCH,<sup>2</sup> RAINER WEINBERGER,<sup>1</sup> PAUL NULSEN,<sup>1,3</sup> AND KRISTIAN EHLERT<sup>4</sup>

<sup>1</sup>Center for Astrophysics | Harvard and Smithsonian  
 Cambridge, MA 02138, USA

<sup>2</sup>NASA/Goddard Space Flight Center  
 Greenbelt, MD 20771, USA

<sup>3</sup>ICRAR, University of Western Australia, 35 Stirling Hwy., Crawley, WA 6009, Australia

<sup>4</sup>Leibniz-Institut für Astrophysik Potsdam (AIP), An der Sternwarte 16, 14482 Potsdam, Germany

### ABSTRACT

Radio relics in galaxy clusters are extended synchrotron sources produced by cosmic-ray electrons in the  $\mu$ G magnetic field. Many relics are found in the cluster periphery and have a cluster-centric, narrow arc-like shape, which suggests that the electrons are accelerated or re-accelerated by merger shock fronts propagating outward in the intracluster plasma. In the X-ray, some relics do exhibit such shocks at the location of the relic, but many do not. We explore the possibility that radio relics trace not the shock fronts but the shape of the underlying distribution of seed relativistic electrons, lit up by a recent shock passage. We use magnetohydrodynamic simulations of cluster mergers and include bubbles of relativistic electrons injected by jets from the central AGN or from an off-center radio galaxy. We show that the merger-driven gas motions (a) can advect the bubble cosmic rays to very large radii, and (b) spread the relativistic seed electrons preferentially in tangential direction – along the gravitational equipotential surfaces – producing extended, filamentary or sheet-like regions of intracluster plasma enriched with aged cosmic rays, which resemble radio relics. Once a shock front passes across such a region, the sharp radio emission edges would trace the sharp boundaries of these enriched regions rather than the front. We also show that these elongated cosmic ray features are naturally associated with magnetic fields stretched tangentially along their long axis, which could help explain the high polarization of relics.

*Keywords:* galaxy clusters — magnetohydrodynamic simulations — extragalactic radio sources — intracluster medium

### 1. INTRODUCTION

During a merger of galaxy clusters, the kinetic energy of the colliding plasma clouds (the intracluster medium, ICM) is dissipated into heat via shock waves and turbulence, with a small fraction of it diverted into amplification of magnetic fields and acceleration of cosmic ray (CR) particles that coexist within thermal plasma. Synchrotron radio emission from the ICM indicates the presence of ultrarelativistic cosmic ray electrons with  $\gamma \sim 10^3 - 10^4$  and magnetic fields of  $B \sim 0.1 - 10 \mu$ G. The brightest sources are the radio lobes associated with active galactic nuclei (AGN), particularly at the centers of massive clusters. Jets from the central black hole

(BH) fill these lobes, inflating giant cavities as they displace the hot ICM, which emits in the X-ray band.

Other diffuse radio sources have no related compact source and their nature is less clear. These sources fall into broad categories of radio halos and radio relics (van Weeren et al. 2019). Radio halos are volume-filling, unpolarized, and diffuse, and are thought to arise from the reacceleration of CRs with  $\gamma \sim 10^2$  (which have long cooling times) by cluster turbulence driven by mergers (Brunetti & Lazarian 2007; Brunetti & Jones 2014; ZuHone et al. 2013). “Giant” halos are seen in clusters undergoing major mergers, with typical sizes of  $\sim 1$  Mpc, while “mini-halos” are seen in the cool cores of relaxed clusters. Radio relics are peripheral, elongated (often in the shape of cluster-centric narrow arcs), strongly polarized sources. Some are associated with shock fronts in the ICM seen in X-rays. Radio relics are further sub-

divided into “gischts”, “phoenixes”, and “AGN relics” (Kempner et al. 2004; van Weeren et al. 2019). AGN relics are fossil plasma from AGN-blown lobes that is passively cooling. Phoenixes are presumed to arise from reacceleration of the aged CRe that originally filled the radio lobes and were subsequently mixed into the ICM by bulk motions and turbulence; a few sources that fit this scenario have been discovered recently at low radio frequencies with *LOFAR* (van Weeren et al. 2019).

Radio gischts in Kempner et al. (2004) terminology, or “radio shocks” in van Weeren et al. (2019) terminology, are often observed at large distances from the cluster center ( $\sim 1 - 2$  Mpc). Many are very long ( $\sim$ Mpc), narrow arcs concentric with the cluster, such as the Sausage relic (van Weeren et al. 2010; Hoang et al. 2017), and some have counterparts on the opposite side of the cluster. It has been assumed that they mark the location of shock fronts (perhaps from a cluster merger) propagating in the ICM, which should accelerate the ICM electrons to ultrarelativistic energies via first-order Fermi process. The high- $\gamma$  electrons should cool rapidly after the shock passage, resulting in narrow ( $\sim$ 100 kpc) radio features. This simple scenario is problematic on energy grounds — if the observed power spectrum of the relativistic electrons is extrapolated down to thermal energies, it would imply an energy in relativistic electrons comparable to the plasma thermal energy (e.g., Macario et al. 2011) and thus an implausibly high acceleration efficiency for the low-Mach ( $\mathcal{M} \lesssim 3$ ) cluster merger shocks. The ICM should contain a population of long-lived relativistic CRe with lower  $\gamma \sim 10^2$  from past acceleration events (Sarazin 1999); it is more likely that shocks re-accelerate those electrons (Markevitch et al. 2005; Kang & Ryu 2016).

However, there are other problems with radio relics occurring at the location of the shocks. While a number of relics do exhibit ICM shocks in the X-ray exactly at the relic “front edges” as expected in the simple acceleration (or re-acceleration) picture (e.g., Giacintucci et al. 2008; Finoguenov et al. 2010; Macario et al. 2011; Shimwell et al. 2015), others do not. For example, at the location of the most prominent and well-studied CIZA J2242.8+5301 Sausage relic (van Weeren et al. 2010), there is no shock in either *Chandra* or *XMM* X-ray images (Ogurcan et al. 2013, 2014; Markevitch et al. 2020). A shock with the required  $M \approx 2.7 - 4.6$  (Hoang et al. 2017) would have been seen in those high-resolution images as easily as that in the Bullet cluster ( $M \sim 3$ ). It is also difficult to explain the morphology of the Sausage relic. A shock front propagating outward is roughly a spherical shell; if it passes through a field of uniformly distributed seed electrons and re-accelerates

them, the radio relic would look like an umbrella in projection rather than a sausage (van Weeren et al. 2011). Furthermore, the Sausage relic is highly polarized (50–60% polarization fraction, van Weeren et al. (2010)). Assuming the magnetic field in the ICM is tangled at random, plasma compression by a shock passage would not be able to create such a highly ordered post-shock field. Indeed, a  $M \sim 3$  shock front in the Bullet cluster produces enhanced radio emission but no detectable post-shock polarization (Shimwell et al. 2014). Some of these issues may be potentially explained by the presence of MHD turbulence upstream of the shock, as noted by Domínguez-Fernández et al. (2020).

We wish to explore an alternative possibility that radio relics such as the Sausage trace the nonuniform distribution of the seed electrons rather than the ICM shocks. We imagine that the ICM at the cluster periphery contains regions polluted with aged relativistic electrons, that those regions have sharp boundaries and shapes as long arched filaments or sheets concentric with the cluster, and that the magnetic fields within those regions are stretched along the filaments. A shock passage across such a region would create a radio relic with all the observed relic properties. We may catch the shock front while it crosses such a region, creating a radio relic at the shock position. When the shock moves out (but not too far, in order to satisfy the electron cooling timescale constraint), the relic “front edge” would delineate the sharp boundary of the polluted region. This is essentially a “phoenix” scenario in the van Weeren et al. (2019) terminology, except more ordered, bigger, brighter and found further out in the clusters. Unlike the shock-compressed relativistic fossils proposed by Enßlin & Gopal-Krishna (2001), these regions would be dominated by thermal plasma with the relativistic electrons providing a small fraction of the total pressure (though higher than elsewhere in the cluster), so shock propagation would not be affected by the relativistic component.

We know that the aged relativistic electrons should be distributed non-uniformly in the ICM and that their distribution affects the radio features. For example, two X-ray shocks in the Bullet cluster have similar Mach numbers but produce very different radio features — one produces a bright radio relic (Shimwell et al. 2015), while the other a much fainter edge of the radio halo (Shimwell et al. 2014). The difference is the radio galaxy near the relic that is likely to have enriched the local ICM with seed electrons and possibly even connected to the relic. Other examples where a radio galaxy apparently feeds the relic have been observed (e.g., van Weeren et al. 2017).

Here, we want to see if gas motions in a merging cluster could naturally produce such narrow, relic-shaped regions enhanced with relativistic particles. To test this possibility, we perform magnetohydrodynamical simulations of galaxy cluster mergers with bubbles, which would be produced either by the central AGN or a radio galaxy at a larger radius. We will show that in some cases, the gas motions can be fast and widespread enough to advect the bubble material from the cluster core to very large radii, and produce large, elongated ( $\sim 1$  Mpc), cluster-centric CR-enriched regions that resemble radio relics such as the Sausage. We also show that in these regions, magnetic fields are naturally stretched tangentially along the filaments, helping to explain the large degree of polarization in relics.

We perform this study using two methods. In the first, we fire jets from a black hole at the center of the cluster, which produces highly magnetized buoyant bubbles near the cluster center which then rise. In the second method, we evacuate a single bubble outside the cluster core (but still much closer to the cluster center than where the peripheral relics are found), to represent the possibility that a local radio galaxy injects CRe into the ICM at that location. In both cases, the bubbles begin to rise but are also advected by the gas motions, and eventually their material is mixed with the ICM. Using a passive scalar field which represents the CRe, we then follow the evolution of this material over time to determine which features are produced.

This paper is organized as follows. Section 2 describes the details of the setup of the simulations, including the cluster mergers, jets, and bubbles. In Section 3, we present our results. In Section 4 we summarize our results and present our conclusions. We assume a  $\Lambda$ CDM cosmology with  $h = 0.7$ ,  $\Omega_m = 0.3$ , and  $\Omega_\Lambda = 0.7$ .

## 2. METHODS

We present two types of binary cluster merger simulations in this work: one with a central AGN in the main cluster which is modeled by a bi-directional jet, and another within which a single bubble is evacuated at a distance from the cluster center. The setup of the initial profiles and orbit of the two clusters, which is the same for both simulation types, is discussed first, followed by the details particular to each simulation.

### 2.1. Initial Condition Setup

In all simulations, the gas in each cluster is modeled as a magnetized, fully ionized ideal fluid with  $\gamma = 5/3$  and mean molecular weight  $\mu = 0.6$ , which is in hydrostatic equilibrium with a virialized dark matter halo which dominates the mass of the cluster. Both clusters

are then situated within a larger computational domain at a distance from each other and given initial velocities. We use the same method for generating these initial conditions for these mergers as in previous works (Ascasibar & Markevitch 2006; ZuHone et al. 2010, 2016, 2018, 2019). We outline this method in brief here.

Our merging clusters consist of a large, “main” cluster, and a smaller infalling subcluster. For the dark matter density profile of the clusters we have chosen a Hernquist (1990) profile:

$$\rho_{\text{DM}}(r) = \frac{M_0}{2\pi a^3} \frac{1}{(r/a)(1+r/a)^3} \quad (1)$$

where  $M_0$  and  $a$  are the scale mass and length of the DM halo. The Hernquist profile has the same dependence on radius in the center as the well-known NFW profile (Navarro, Frenk, & White 1997),  $\rho_{\text{DM}} \propto r^{-1}$  as  $r \rightarrow 0$ , but is used here instead because it is more analytically tractable and its mass profile converges as  $r \rightarrow \infty$ .

For the gas density, we use a phenomenological formula which can model cool-core clusters with temperature decreasing towards the cluster center (Ascasibar & Markevitch 2006):

$$\rho_{\text{gas}}(r) = \rho_{g0} \left(1 + \frac{r}{a_c}\right) \left(1 + \frac{r/a_c}{c}\right)^\alpha \left(1 + \frac{r}{a}\right)^\beta, \quad (2)$$

with exponents

$$\alpha \equiv -1 - n \frac{c-1}{c-a/a_c}, \quad \beta \equiv 1 - n \frac{1-a/a_c}{c-a/a_c}, \quad (3)$$

where  $0 < c < 1$  is a free parameter that characterizes the depth of the temperature drop in the cluster center and  $a_c$  is the characteristic radius of that drop, or the “cooling radius”. We set  $n = 5$  in order to have a constant baryon fraction at large radii, and we compute the value of  $\rho_0$  from the constraint  $M_{\text{gas}}/M_{\text{DM}} = \Omega_{\text{gas}}/\Omega_{\text{DM}} = 0.12$ . With this density profile and Equation 1, the corresponding gas temperature can be derived by imposing hydrostatic equilibrium.

We employ two different merger scenarios in our study, which vary only in the properties of the subcluster. In the first simulation (called “Merger1”), the mass ratio of the two clusters is  $R \equiv M_1/M_2 = 5$  and the subcluster only possesses dark matter. This setup produces relatively gentle sloshing gas motions that persist for many Gyr. The second simulation (called “Merger2”) has  $R = 3$  and the subcluster is also a cool-core cluster. This simulation produces very fast and turbulent gas motions.

The mass of the main cluster is  $M_1 = 1.25 \times 10^{15} M_\odot$  in both simulations. To scale the initial profiles for the two subclusters, the combination  $M_i/a_i^3$  in Equation 1

is held constant. For the main cluster, we chose  $a_1 = 600$  kpc,  $c_1 = 0.17$ , and  $a_{c1} = 60$  kpc, to resemble mass, gas density, and temperature profiles typically observed in massive, relaxed cool-core clusters. In the “Merger2” simulation, its gas properties are set assuming  $c_1 = c_2$  and  $a_{c1}/a_1 = a_{c2}/a_2$ . We will describe the post-merger properties of the two simulations in detail in Section 3.1.

For all simulations, the clusters start at a separation of  $d = 3$  Mpc, and with an initial impact parameter  $b = 500$  kpc. The initial cluster velocities are chosen so that the total kinetic energy of the system is set to half of its potential energy, under the approximation that the objects are point masses. This results in a relative velocity of  $v_{\text{rel}} \sim 1100$  km s $^{-1}$ .

Finally, the gas in each cluster is also magnetized. To set up the initial magnetic field we follow the procedure from Brzycki & ZuHone (2019) and references therein. Briefly, we set up a divergence-free turbulent magnetic field on a uniform grid with a Kolmogorov spectrum which is isotropic in the three spatial directions. The average magnetic field strength is scaled to be proportional to the square root of the thermal pressure such that  $\beta = p_{\text{th}}/p_B$  is constant. The magnetic field components are then interpolated from this grid onto the cells in each simulation.

## 2.2. Simulation Code Details

### 2.2.1. AREPO Jet Simulations

The AREPO code (Springel 2010) employs a finite-volume Godunov method on an unstructured moving Voronoi mesh to evolve the equations of magnetohydrodynamics (MHD), and a Tree-PM solver to compute the self-gravity from gas and dark matter. The magnetic fields are evolved on the moving mesh using the Powell 8-wave scheme with divergence cleaning employed in (Pakmor & Springel 2013) and in the IllustrisTNG simulations (Marinacci et al. 2018). These simulations also include dark matter particles, which make up the bulk of the cluster’s mass and only interact with each other and the gas via gravity.

The particle and Voronoi cell properties in the simulations are set by the initial profiles described in 2.1, with their initial velocities set to zero in the rest frame of their cluster. The initial magnetic field is set according to the procedure outlined above in Section 2.1 assuming  $\beta = 100$ . The DM particles all have the same mass. The gas cells are initialized to all have the same mass, though they are allowed to undergo mesh refinement and derefinement during the simulation evolution, so this condition will not remain strictly true in their case as the simulation progresses. For each of the particle/cell positions, a random deviate  $u = M(< r)/M_{\text{total}}$

is uniformly sampled in the range [0,1]. Given  $u$ , inverting the function  $M(< r)/M_{\text{total}}$  gives the radius of the particle/cell from the center of the halo.

For the DM particles, their initial velocities are determined using the procedure outlined in Kazantzidis et al. (2004), which computes the particle speed distribution function directly using the method of Eddington (1916). Once the particle radii and speeds are determined, positions and velocities are determined by choosing random unit vectors in  $\mathbb{R}^3$ .

The AREPO simulations are set within a cubical computational domain of width  $L = 40$  Mpc on a side, though for all practical purposes the region of interest is confined to the inner  $\sim 10$  Mpc. Before each simulation, we also perform a mesh relaxation step for  $\sim 100$  timesteps to prevent spurious gas density and pressure fluctuations from forming due to the random nature of the initial condition.

The gas cells in each simulation initially have mass  $m_{\text{gas}} = 1.14 \times 10^7 M_{\odot}$ , though these can change with refinements and derefinements of cells. The DM particles have mass  $m_{\text{DM}} = 9.95 \times 10^7 M_{\odot}$ . The main cluster in both simulations has  $10^7$  DM particles, and initially has  $10^7$  gas cells. The subcluster in the “Merger1” simulation contains  $1.97 \times 10^6$  DM particles. The subcluster in the “Merger2” simulation contains  $3.57 \times 10^6$  DM particles, and initially has  $3.61 \times 10^6$  gas cells. The gravitational softening length for the gas cells and the DM particles is 2 kpc.

For simulating the effects of AGN in the AREPO simulations we use the method of Weinberger et al. (2017). This method injects a bi-directional jet which is kinetically dominated, low density, and collimated. Kinetic, thermal, and magnetic energy is injected into two small spherical regions a few kpc from the location of a black hole particle. The material injected by the jet is marked by a passive tracer field  $\rho_{\text{CR}}$  (which represents the CRe-enriched material) and is advected along with the fluid for the rest of the simulation. For the purposes of this preliminary study, other effects which are important to the evolution of CRe, such as diffusion, streaming, (re)acceleration, and cooling are ignored, but will be pursued in later works.

A black hole particle is placed at the cluster potential minimum. This particle has a mass of  $M_{\text{BH}} = 3 \times 10^9 M_{\odot}$ . Since we perform no accretion onto the black hole particle in our simulations, the precise value of the mass is of little importance, with the exception that it must be large enough to not be affected significantly by interactions with DM particles and remain at the cluster potential minimum.

The black hole particle serves as the site of the jet injection by the AGN. In each simulation, the jets are fired with a power  $P_{\text{jet}} = 3.169 \times 10^{45} \text{ erg s}^{-1}$  for a duration of  $t_{\text{jet}} = 100 \text{ Myr}$ , so the resulting total energy injected is  $E_{\text{jet}} = 10^{61} \text{ erg}$  in each direction, which is a sum of kinetic, thermal, and magnetic energy. In the jet region, the magnetic and thermal pressures are equal ( $\beta_{\text{jet}} = P_{\text{th}}/P_B = 1$ ), and the injected magnetic field is purely toroidal.

### 2.2.2. *FLASH* Bubble Simulations

The *FLASH* code evolves the MHD equations on a structured adaptive mesh refinement (AMR) grid, a method of partitioning a grid throughout the simulation box such that higher resolutions (smaller cell sizes) are only used where needed. On this mesh, *FLASH* uses a directionally unsplit staggered mesh algorithm (USM; Lee & Deane 2009). The USM algorithm used in *FLASH* is based on a finite-volume, high-order Godunov scheme combined with a constrained transport method (CT), which guarantees that the evolved magnetic field satisfies the divergence-free condition (Evans & Hawley 1988). In our simulation, the order of the USM algorithm corresponds to the Piecewise-Parabolic Method (PPM) of Colella & Woodward (1984). The gas properties are set by the initial profiles on the AMR cells described in Section 2.1. In this simulation, the initial magnetic field is set according to the procedure outlined above in Section 2.1 assuming  $\beta = 200$ .

The dark matter halos, and the gravitational potentials they produce, are modeled by two rigid Hernquist (1990) potentials which move under the influence of each other's gravity. The gravitational acceleration from the halos is evaluated by finite-differencing the potential on the AMR grid. Because the main cluster is held fixed at the center of the simulation domain in this simulation, an additional acceleration term is added to the grid to account for non-inertial frame effects. This procedure is outlined in more detail in ZuHone et al. (2011) and Roediger & ZuHone (2012). The *FLASH* simulation is set within a cubical computational domain of width  $L = 8 \text{ Mpc}$  on a side, with a finest cell size of  $\Delta x = 0.98 \text{ kpc}$ .

In the *FLASH* simulation, a bubble of radius  $r_{\text{bub}} = 25 \text{ kpc}$  is created at a distance of  $d_{\text{bub}} = 200 \text{ kpc}$  from the cluster center. This may represent a bubble created by an AGN at the cluster center which is extremely stable and rises to this height, or more likely a high-entropy cloud of hot plasma and CR injected by another radio galaxy in the cluster at that distance. The bubble is produced by reducing the density within  $r_{\text{bub}}$  and adjusting the temperature such that the pres-

sure within the bubble cells remains constant. This results in a bubble energy of  $E_{\text{bub}} \sim 2 \times 10^{59} \text{ erg}$ . The resulting entropy of the material in the bubble is  $K_{\text{bub}} = k_B T_{\text{bub}} n_{e,\text{bub}}^{-2/3} = 4000 \text{ keV cm}^2$ , higher than the surrounding ICM by a factor of  $\sim 4$ , so that it will buoyantly rise. The magnetic field in the bubble is not changed. Similar to the *AREPO* simulations, the bubble material is also marked with a passive tracer  $\rho_{\text{CR}}$  (which represents the CR-enriched material) to follow its subsequent evolution by its being advected along by the gas motions. Our past experience with simulations of a CR bubble advected by plasma in a sloshing cluster core (ZuHone et al. 2013) suggests that the exact initial shape of the CR cloud, a spherical bubble in this case, is forgotten on a couple of dynamic timescales and has little effect the final morphology.

## 3. RESULTS

### 3.1. *Characteristics of the Merger-Driven Cluster Gas Properties*

Before describing the simulations with the effects of AGN bubbles included, we first detail the properties of the gas within each cluster as a result of the merging activity itself.

The “Merger1” simulation is the same setup as presented in a number of previous works (Ascasibar & Markevitch 2006; ZuHone et al. 2010, 2016, 2018, 2019). A gasless, DM-only subcluster perturbs the center of a relaxed, cool-core cluster and produces sloshing motions. Slices through the merger plane of the temperature and the magnetic field strength for four epochs of this simulation after the first core passage of the subcluster are shown in Figure 1. The sloshing motions develop cold fronts and gas velocities of several hundred  $\text{km s}^{-1}$  in the core region. By the time the jets are switched on at  $t = 5 \text{ Gyr}$ , the largest cold front has propagated out to  $r \sim 250 \text{ kpc}$ , and most of the region inside  $r \lesssim 500 \text{ kpc}$  is caught up in the subsonic spiral motions. These motions have also amplified the magnetic field within the sloshing region (as shown originally in ZuHone et al. 2011) and wound the field lines in a mostly tangential direction. We run this simulation for both the *AREPO*/jet and *FLASH*/bubble cases, though we only show the merger evolution of the former case in Figure 1.

Slices through the merger plane of the temperature and the magnetic field strength for four epochs of the “Merger2” simulation after the first core passage of the subcluster are shown in Figure 2. In this simulation, a gas-filled subcluster only three times smaller than the main cluster passes near the cluster core, driving shocks and large-scale bulk motions up to  $\sim 1000 \text{ km s}^{-1}$  in the core region. These motions produce large cold fronts

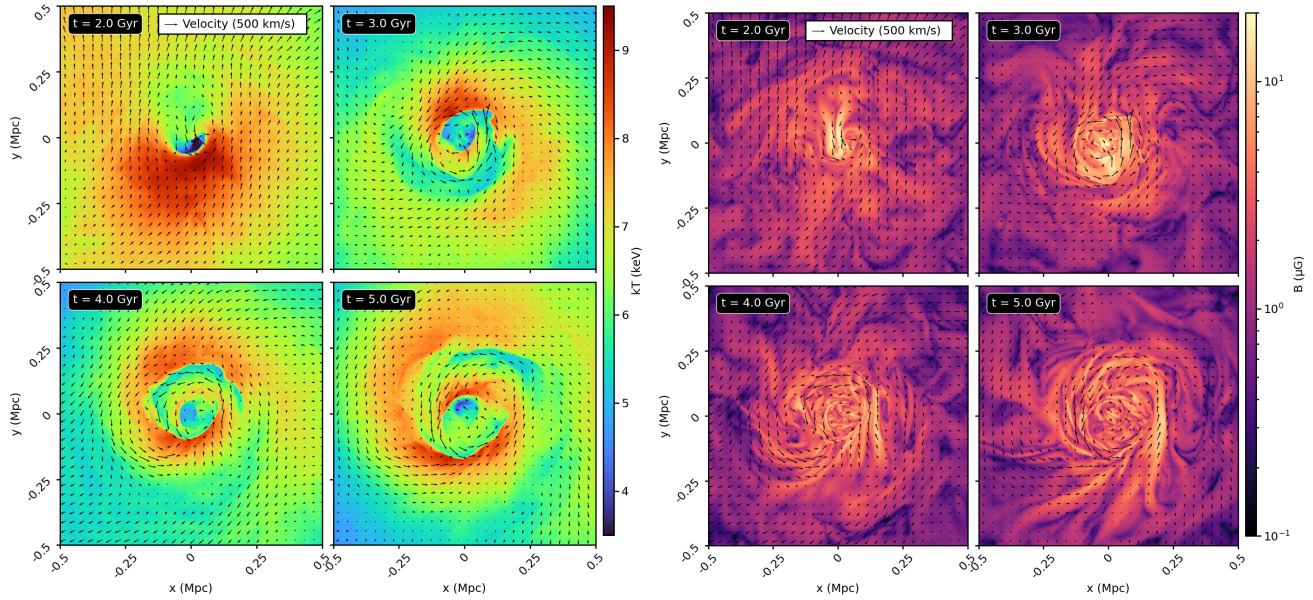


**Figure 1.** Slices of the gas temperature (left) and the magnetic field strength (right) for four different epochs in the “Merger1” simulation, centered on the cluster potential minimum. Velocity vectors in the slice plane are also shown. The AGN is turned on at the last snapshot shown here.

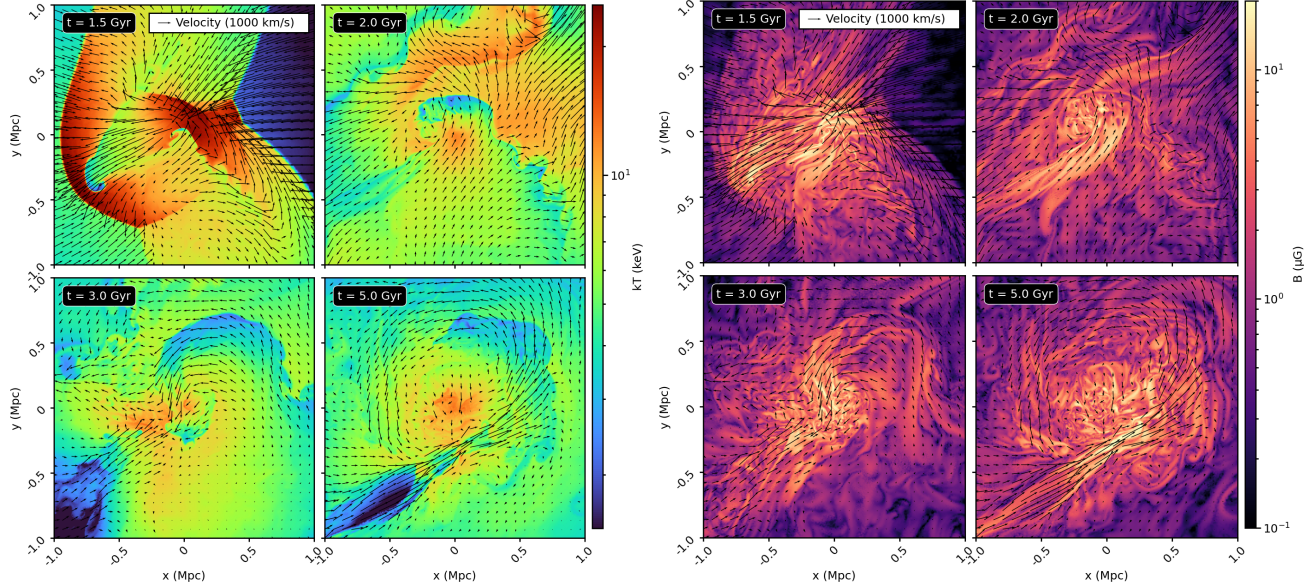


**Figure 2.** Slices of the gas temperature (left) and the magnetic field strength (right) for four different epochs in the “Merger2” simulation, centered on the cluster potential minimum. Velocity vectors in the slice plane are also shown.

which propagate to large radii of  $r \sim 700$  kpc. At later times ( $t \sim 3 - 5$  Gyr), the subcluster makes its second core passage, driving a fast, highly magnetized, cold inflow of gas to the south of the core. The gas motions and magnetic field in the core region are highly turbulent by  $t = 5.0$  Gyr.

### 3.2. Evolution of the Spatial Distribution of the Bubble Material

We implement the effects of AGN in all of the merger simulations at  $t = 5$  Gyr,  $\Delta t \sim 3.5$  Gyr after the first core passage. For the description of the simulations from this point on, the times will be measured in terms of  $\tau = t - t_{\text{AGN}}$  where  $t_{\text{AGN}} = 5$  Gyr. At this point, in all simulations the gas motions are well-developed, as shown in the previous section.

#### 3.2.1. The “Merger1”/jet Simulations

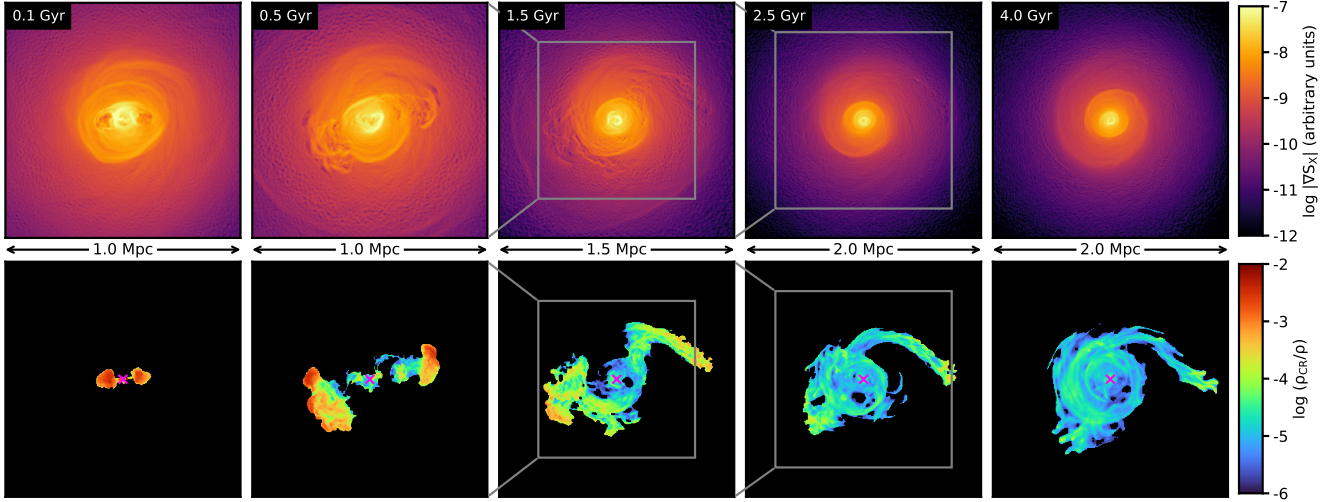


**Figure 3.** The evolution of the “Merger1”/jet simulation for the first 4 Gyr after jet ignition, with jets aligned along the  $x$ -axis. The top panels show projected X-ray surface brightness gradient, and the bottom panels show projected CR fraction. The physical width of each panel expands from left to right, indicated by the scale bars and the inset boxes. The magenta “x” marks the cluster center in the bottom panels. All projections are along the  $z$ -axis.

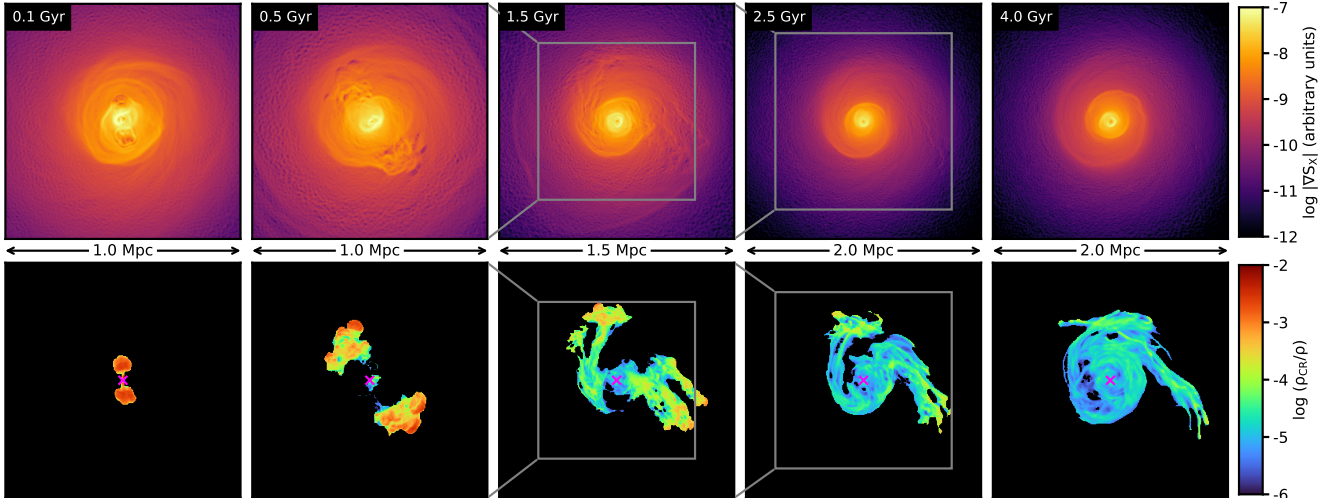


**Figure 4.** The evolution of the “Merger1”/jet simulation for the first 4 Gyr after jet ignition, with jets aligned along the  $y$ -axis. The time labels show  $\tau = t - t_{\text{AGN}}$ , where  $t_{\text{AGN}} = 5$  Gyr. The top panels show projected X-ray surface brightness gradient, and the bottom panels show projected CR fraction. The physical width of each panel expands from left to right, indicated by the scale bars and the inset boxes. The magenta “x” marks the cluster center in the bottom panels. All projections are along the  $z$ -axis.

The evolution of the jet-injected material in the “Merger1” simulations is shown in Figures 3 (jets in the  $x$ -direction) and 4 (jets in the  $y$ -direction). The top panels in these figures (and following ones) show the gradient of X-ray surface brightness as computed using the Gaussian Gradient Magnitude (GGM) technique (Sanders et al. 2016; Walker et al. 2016). This allows sharp features such as cold fronts and bubbles to be shown more clearly. At the end of the jet injection at  $\tau = 0.1$  Gyr, two bubbles with diameters of  $\sim 70$  kpc,

separated by  $\sim 130$  kpc, are visible as cavities in the X-ray and as enhancements in the projected bubble distribution (left-most panels of Figures 3 and 4). By  $\tau = 0.5$  Gyr the bubbles have risen to radii of  $\sim 200$ -300 kpc, and have dragged cold, dense, and highly magnetized gas from the core outward in their wakes. The sloshing motions have already noticeably displaced the bubbles away from the original jet axis. At this point, the bubbles are starting to become disrupted by gas turbulence and instabilities, and their material (and the gas they

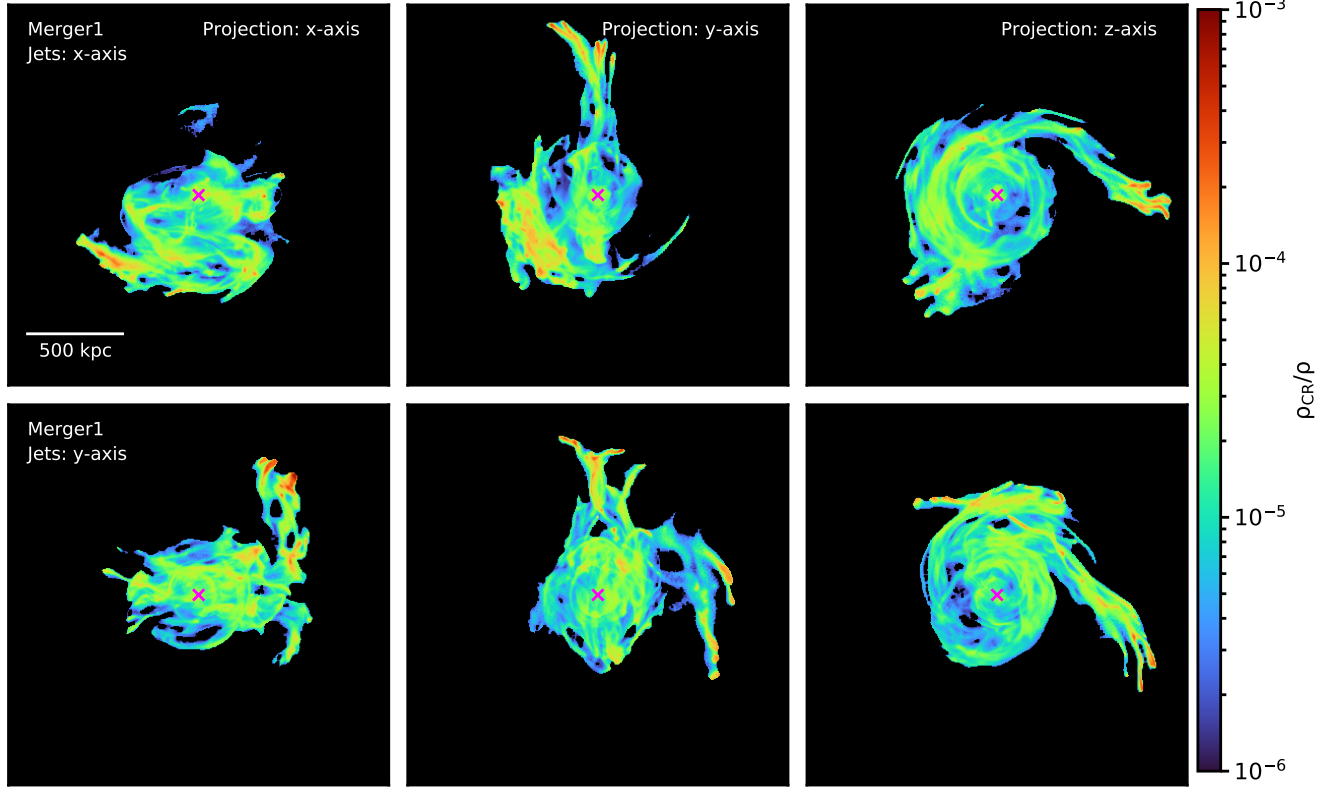


**Figure 5.** The projected CR distribution along the principle axes of the simulation box for the “Merger1”/jet simulations, for both cases of the jet direction, at  $\tau = 4$  Gyr. The position of the cluster center is marked by a magenta “x”.

have entrained behind them) is beginning to mix with the surrounding ICM. As the simulation proceeds to  $\tau = 1.5$  Gyr, the sloshing gas motions begin to spread the bubble material around in a tangential direction.

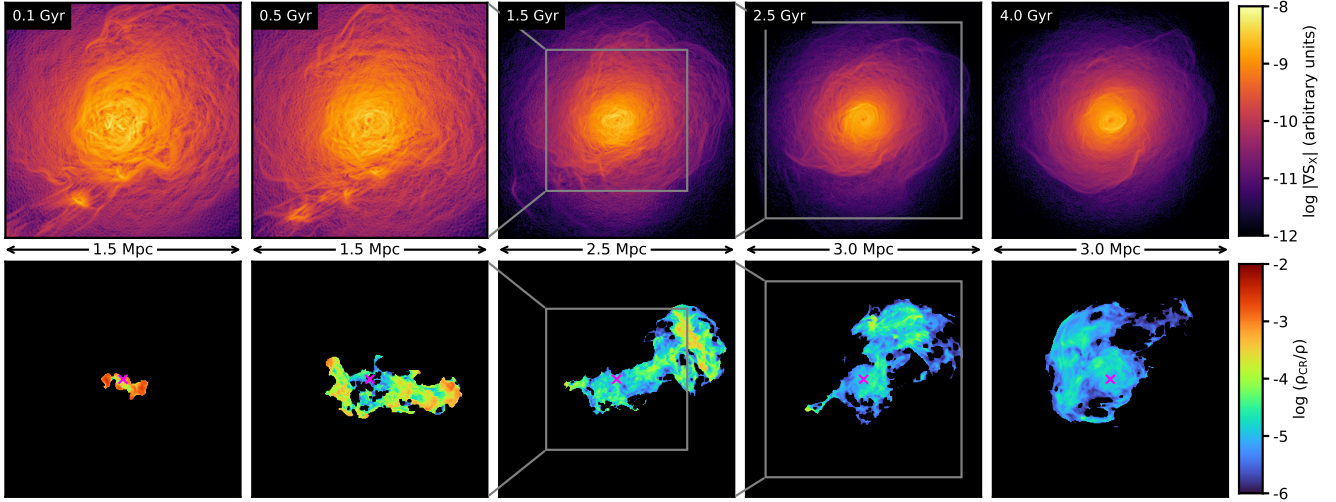
At later stages ( $\tau \gtrsim 1.5$  Gyr in Figures 3 and 4), the bubble material’s rise is significantly slowed as it has become thoroughly mixed with the cluster ICM and its entropy is lowered. The merger-driven gas motions now dominate its evolution, resulting in two effects. The first is that the central volume of  $\sim 200$ - $300$  kpc bounded by the sloshing cold fronts is filled uniformly with bubble material. This effect is interesting, as it provides another reason why we may expect radio mini-halo emission to be confined by cold fronts if the CRs are re-accelerated by turbulence, as first noted by Mazzotta & Giacintucci (2008) and simulated in ZuHone et al. (2013). Secondly, the outermost gas motions produce long, relatively straight or arc-like strips of bubble material which extend and evolve to larger radii of  $\sim 500$ - $700$  kpc. These strips have sharp boundaries reminiscent of radio relics. In the plane of the sky parallel to the gas motions, these strips have a width of  $\sim 100$ - $200$  kpc.

Figure 5 shows the bubble distribution projected along the three principal axes of the “Merger1” simulations. Along all three projections, the core region inside  $r$

200 kpc is filled nearly uniformly with CRs, with filamentary structures with sharp boundaries extending out to roughly  $\sim 500$ - $700$  kpc in various directions. The width of these extensions clearly depends on the projection angle.

### 3.2.2. The “Merger2”/jet Simulations

The evolution of the jet-injected material in the “Merger2” simulations is shown in Figures 6 (jets in the  $x$ -direction) and 7 (jets in the  $y$ -direction). In these simulations, the bubbles are disrupted far more quickly than in the “Merger1” simulation by the faster and more turbulent motions. This leads in the long term to a more diffuse distribution of the bubble material than in the “Merger1” simulations. There is a very fast cold flow largely in the  $+x$ -direction which begins to the southeast of the core and ends west of it before it curves up and eventually counterclockwise around the core. By  $\tau = 0.5$  Gyr, the bubble material has been caught up within this flow such that it has spread nearly  $\sim 0.7$  Mpc in the western direction, whereas it has barely expanded on the other side of the core in the eastern direction. This is even true in the case of the simulation with the jets in the  $y$ -direction, where the bubble launched to the south has been essentially immediately pushed  $90^\circ$



**Figure 6.** The evolution of the “Merger2”/jet simulation for the first 4 Gyr after jet ignition, with jets aligned along the  $x$ -axis. The top panels show projected X-ray surface brightness gradient, and the bottom panels show projected CR fraction. The physical width of each panel expands from left to right, indicated by the scale bars and the inset boxes. The magenta “x” marks the cluster center in the bottom panels. All projections are along the  $z$ -axis.

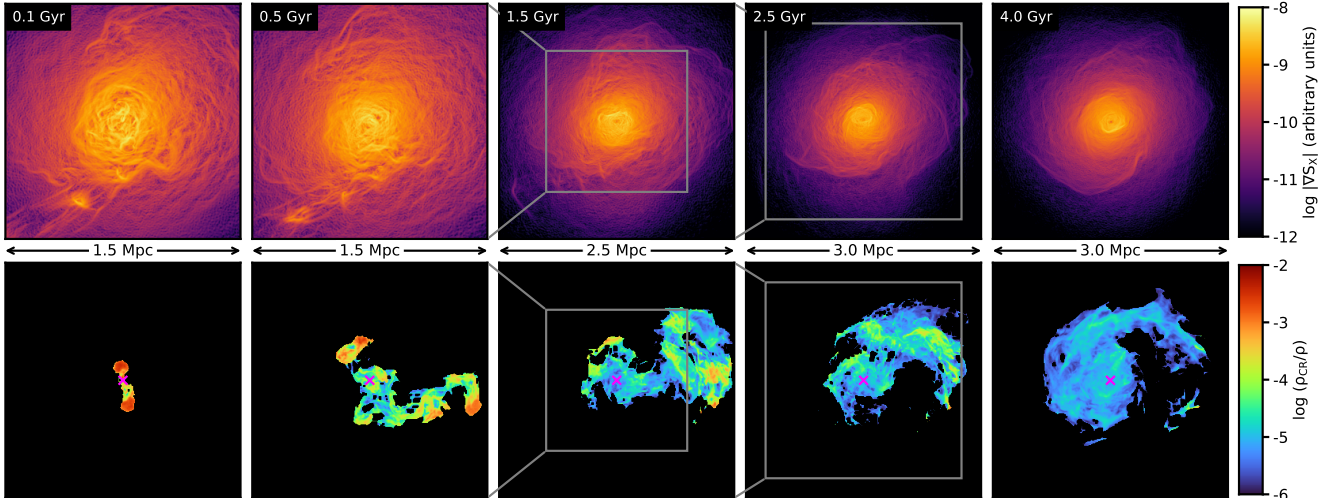


**Figure 7.** The evolution of the “Merger2”/jet simulation for the first 4 Gyr after jet ignition, with jets aligned along the  $y$ -axis. The top panels show projected X-ray surface brightness gradient, and the bottom panels show projected CR fraction. The physical width of each panel expands from left to right, indicated by the scale bars and the inset boxes. The magenta “x” marks the cluster center in the bottom panels. All projections are along the  $z$ -axis.

from its original direction of motion by the fast flow. By  $\tau \sim 1.5$  Gyr in both simulations, the bubble material has spread westward out to a radius of  $\sim 1.2$  Mpc, and northward by a distance of  $\sim 0.8$  Mpc.

At later times, from  $\tau \sim 2.5 - 4$  Gyr, the bubble material is completely caught up in the large-scale bulk motions in the northwest direction from the core, which spread them out in a large wide arc, with a span of  $\sim 1.5$  Mpc, in a spiral pattern. These are again confined by the large, sloshing-type motions in this direction, so they have mostly well-defined edges. However, the dis-

tribution of bubble material is more diffuse and spread out within these regions than in the “Merger1” simulations.

Figure 8 shows the bubble material distribution projected along the three principal axes of the “Merger2” simulations. All projections show that this distribution is more diffuse than in the “Merger1” simulations. The outward sharp boundaries of the CR distribution are ubiquitous.

### 3.2.3. The “Merger1”/bubble Simulation

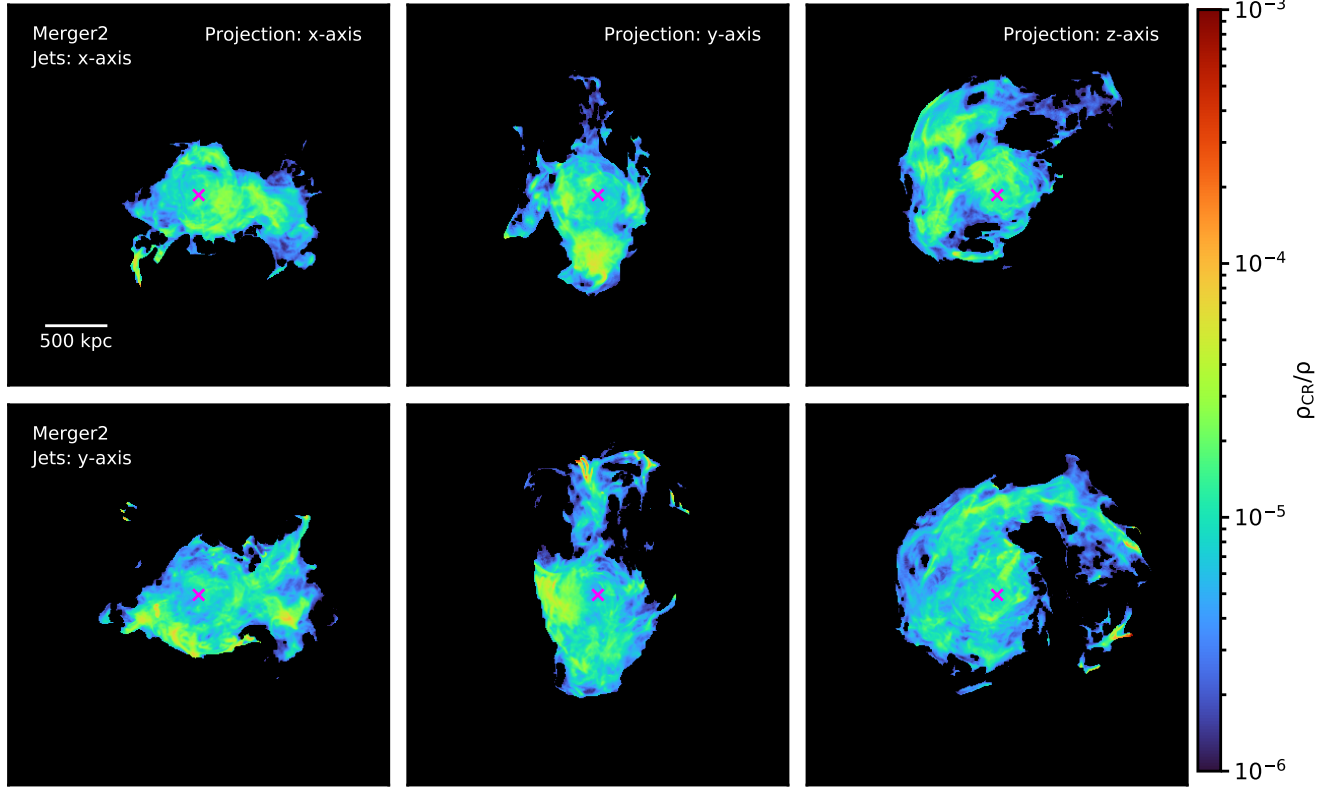


**Figure 8.** The projected CR distribution along the principle axes of the simulation box for the “Merger2”/jet simulations, for both cases of the jet direction, at  $\tau = 4$  Gyr. The position of the cluster center is marked by a magenta “x”.

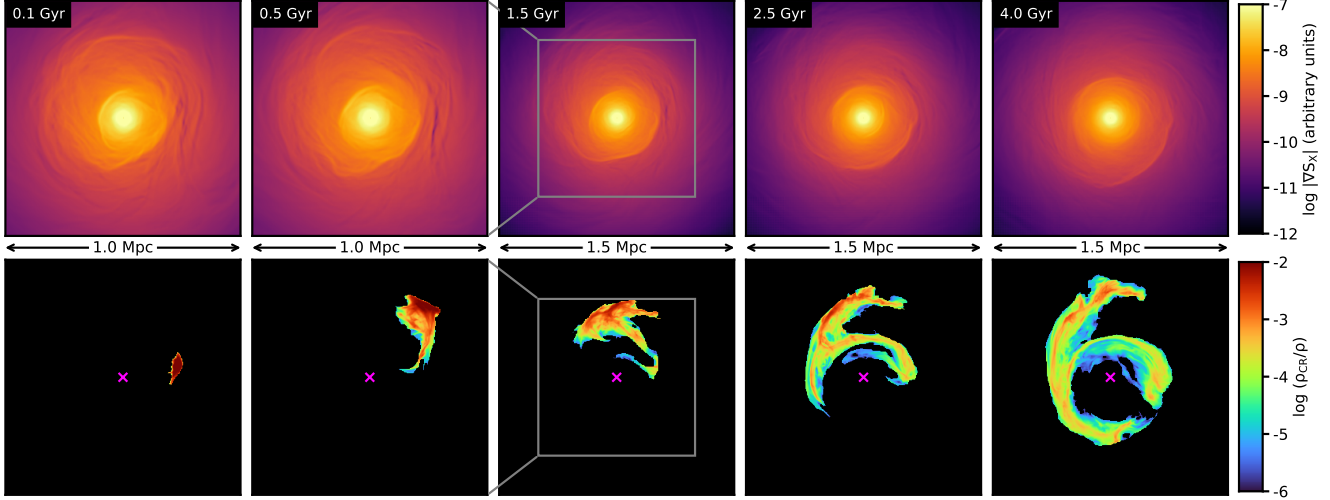
As mentioned in Section 2.2.2, in this simulation a single high-entropy bubble is inserted at a radius of 200 kpc from the cluster center, perhaps injected into the ICM by a local radio galaxy. The evolution of this simulation is shown in Figure 9. The bubble begins to rise buoyantly and flattens out in the tangential direction. It becomes quickly caught up in the sloshing motions as it rises, so that by  $\tau \sim 1.5$  Gyr it has already spread out over a tangential distance of  $\sim 0.75$  Mpc. At this epoch, a small amount of the bubble material, which has become effectively mixed with lower-entropy gas originally dragged upward by the bubble, begins to fall back toward its original radius, and spreads around in the tangential direction. The still-higher entropy bubble material continues to rise, but continues to spread over a large tangential distance. Lower-entropy material has settled at a radius of  $r \sim 200 - 400$  kpc, and has nearly spread around in a complete circle by  $\tau \sim 4$  Gyr.

Figure 10 shows the projected bubble material along the three coordinate axes of the simulation domain at the epoch  $\tau = 0.4$  Gyr. Along the  $x$  and  $y$ -projections of the simulation, the material dispersed from the original bubble appears as a very thin line of width  $\sim 100$  kpc, nearly  $\sim 1$  Mpc in length, except in the core region of

radius  $\sim 200$  kpc where the bubble material is starting to be spread around more uniformly.

In this setup, the bubble originally appears undisrupted at large radius with a high concentration of radio plasma. In contrast, in the jet simulations, the bubbles are launched near the cluster center and undergo disruption and mixing with the ICM plasma before they reach the same radius. The result is that in the former simulation, the density of bubble material which is spread around is higher at large radius than in the latter. The two cases differ in morphological detail, but produce common qualitative features in the CR distribution — the ubiquitous elongated, tangential arc-like filaments with well-defined sharp boundaries, located much farther in the cluster periphery than the initial injection sites. We showed results for only one set of initial bubble radii for each simulation; for other radii, the picture is similar but with different linear scales. For jets oriented at different angles in the plane of the sky (along  $x$  and  $y$  axes), there is no qualitative difference in the final CR distribution.

### 3.3. The Distribution of the Magnetic Field in the CR-populated Region



**Figure 9.** The evolution of the “Merger1”/bubble simulation for the first 4 Gyr after bubble placement. The top panels show projected X-ray surface brightness gradient, and the bottom panels show projected CR fraction. The physical width of each panel expands from left to right, indicated by the scale bars and the inset boxes. The magenta “x” marks the cluster center in the bottom panels. All projections are along the  $z$ -axis.

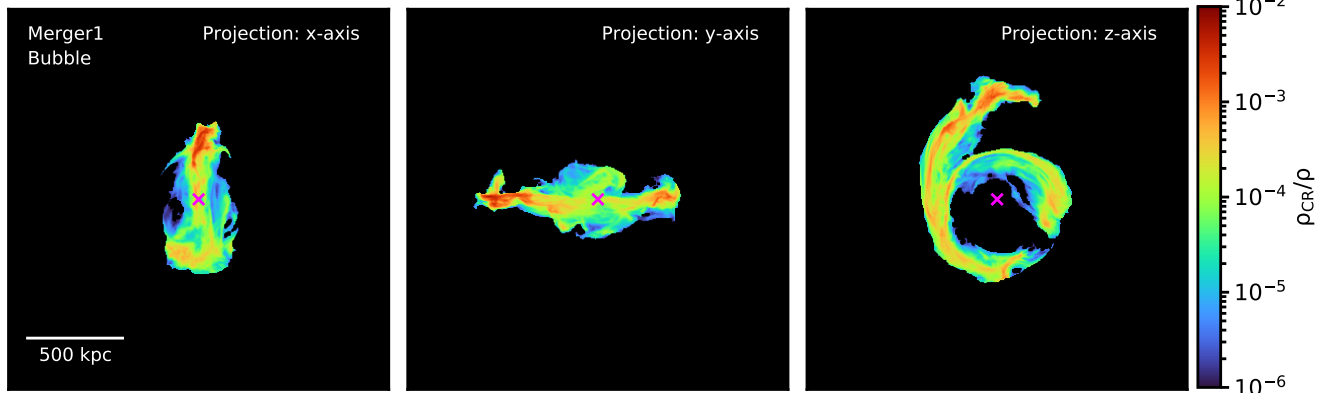


**Figure 10.** The projected CR distribution along the principle axes of the simulation box for the “Merger1”/bubble simulation at  $\tau = 4$  Gyr. The position of the cluster center is marked by a magenta “x”.

Radio relics are usually polarized (Ensslin et al. 1998; van Weeren et al. 2010, 2019), with the polarization direction perpendicular to the long axis of the relic. It is an open question whether or not such magnetic field alignments arise naturally from the process of forming the relic itself, or if relics appear predominantly in regions with magnetic fields oriented tangentially to their surfaces. We can check the orientation of the magnetic field within the elongated CRe regions in our simulations.

In Figure 11 we show the projected CR distribution along the  $z$ -axis of four simulations, with plane-of-sky projected magnetic field vectors overlaid. The projected magnetic field has been weighed by a factor  $B^2 \rho_{\text{CR}}$ , which will be proportional to the monochromatic emis-

sion of a radio relic with  $\alpha = 1$  for  $I(\nu) \propto \nu^{-\alpha}$ . In each of these cases, elongated regions of enhanced CR distribution are associated with magnetic field lines which are largely aligned lengthwise along these features. Such alignments naturally arise due to the fact that the same motions which spread the CRs out over long distances stretch and amplify the magnetic field along the same direction. These magnetic field configurations could be the origin of polarization in these sources, which would be augmented by the passing of weak shock to provide additional field compression and alignment.

#### 4. SUMMARY

This paper represents an initial exploratory step using MHD simulations of galaxy cluster mergers with AGN bubbles in testing the hypothesis that the CRe

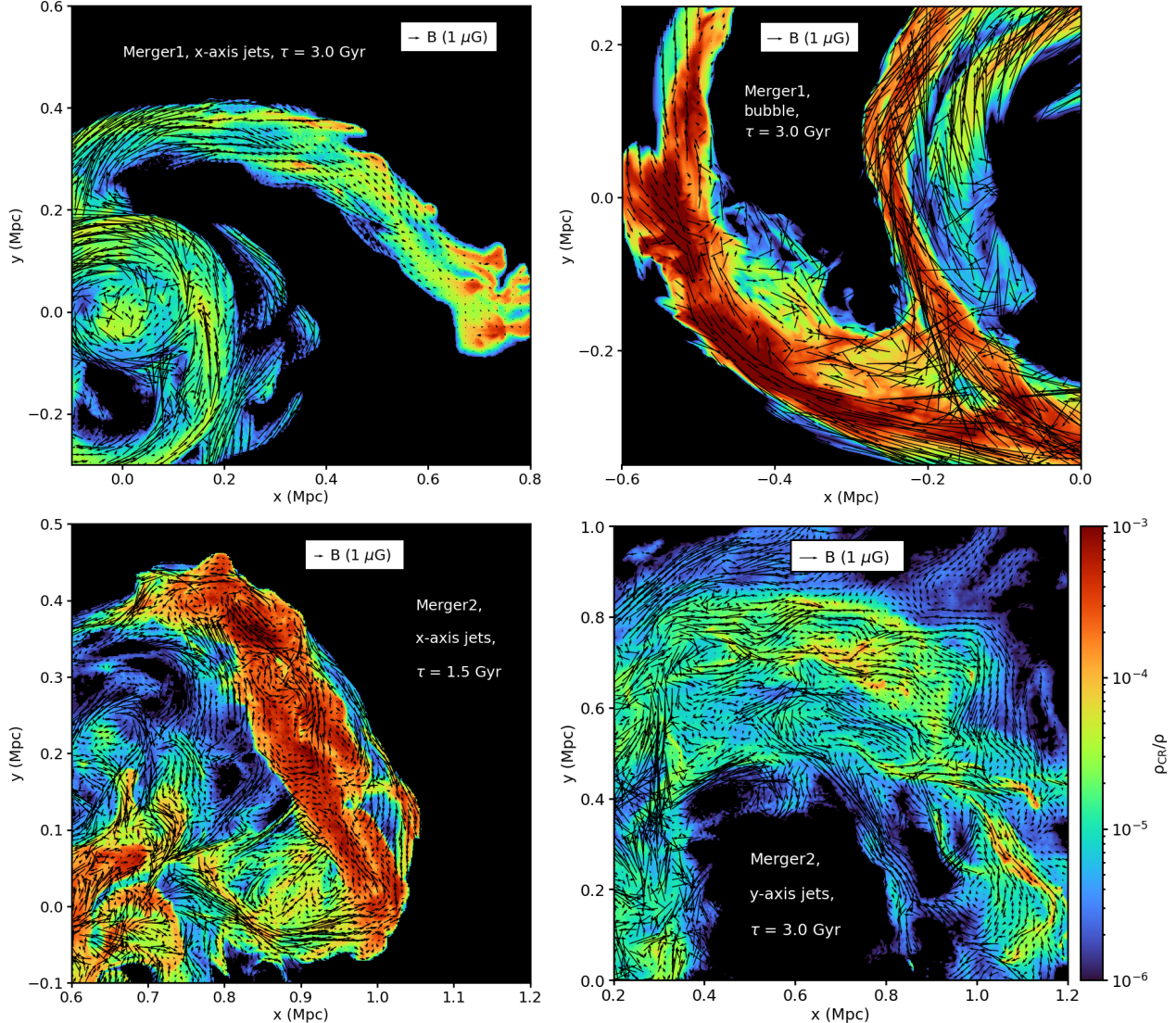


**Figure 11.** Projected CR distribution and plane-of-sky magnetic field vectors in the vicinity of three extended CR regions in four simulations. The magnetic field vectors are weighted proportional to  $B^2 \rho_{\text{CR}}$ .

from AGN-blown bubbles can be turned into radio relics. Specifically, this occurs by the transport of the CRe by merger-driven gas motions to larger radii where they are stretched in the direction tangential to the cluster equipotential surfaces / isophotes. Such CRe can then be reaccelerated by a passing merger shock, explaining the spatial association of the radio features with X-ray detected shocks in some clusters but also explaining why not all radio relics have such associations. In particular, we find that:

- The bubbles produced by jets which emanate from a central AGN are quickly offset (in our simulations, within 0.5 Gyr) from the original jet axis by sloshing gas motions. Faster and more turbulent motions from a more violent merger can offset

bubbles to a greater degree, but these motions also tend to disrupt bubbles rather quickly.

- Cluster mergers which produce relatively gentle sloshing motions can spread bubble material out to relatively large radii, of roughly  $r \sim 0.5 - 0.6$  Mpc. More energetic mergers, which can produce fast-moving bulk motions which quickly develop into turbulence, can spread it to even larger radii, of  $\sim 1$  Mpc.
- The CRe structures produced by these motions in either case can be stretched greatly in the tangential direction,  $\sim 1$  Mpc, especially if the merger occurs with a significant impact parameter, such mergers produce fast motions in the tangential direction. Such spatial distribution is expected in a

stratified, largely centrally-symmetric cluster atmosphere (which is true even for highly disturbed clusters) — a parcel of gas with a given specific entropy spreads much more easily along the isentropic surface than in the radial direction. These same motions will stretch and amplify magnetic fields parallel to these structures, which could potentially explain the polarization of radio relics.

- In mergers where the gas motions are comparatively gentle and less turbulent, such as our “Merger1” simulation, the long tangential regions of enhanced bubble material are very narrow, similar to those seen in many radio relics. In the more turbulent “Merger2” simulation, the regions of enhanced CRe are unsurprisingly wider and more diffuse. Of course, determining whether or not the full region populated by CRe is lit up after a shock passage will require more detailed simulation, including the energetics of the CRe (see below), so it is premature to suggest that sloshing motions produce thin relics and more turbulent motions produce thicker ones.
- In our simulation which used a single bubble at a radius of 200 kpc, the density of bubble material is much larger and it is distributed in more coherent structures than in the simulations where the bubbles are produced by an AGN at the cluster center. This may indicate that thinner and more coherent radio features may be produced by radio galaxies at larger radii which inject CRe locally, but future simulation works with more detailed physics are required to examine this possibility. These simulations should also include more realistic inflation of bubbles, since real bubbles will be born with kinetic energy, momentum, and an internal magnetic field structure, which the method employed in the **FLASH** simulation does not include.
- The core region of the cluster in the jet simulations is quickly filled up with CRe which originated from the AGN, confirming the hypothesis that the central AGN could provide the seed electrons for radio mini-halos (see e.g. [ZuHone et al. 2013](#)).

Such a hypothesis for the origin of radio relics neatly explains several puzzling features:

1. they are not always seen coincident with merger shocks on the sky, since the shock may have run over the CRe-populated region and left, though it should still be nearby given the short cooling times of relativistic electrons

2. why merger shocks do not always produce detectable radio relics, since it is required that the shocks will pass over CRe-populated regions
3. why relics do not always have shapes that resemble merger shocks; in this case, the shape of the relic is simply the shape of the CRe-populated region, which depends on how they were distributed by gas motions.

For our jet-based simulations, a caveat is in order. Observationally, the bubble energy of  $10^{61}$  erg corresponds to the most energetic bubbles observed in clusters, which may not be typical of the history of many clusters with radio relics. Radio jets with less power will generate bubbles with less energy, which will be less capable of rising to large radii in the ICM, and perhaps will not reach the distances required for relic production. This shows why the second scenario we explored, that of radio plasma injected at larger radius, is highly relevant and deserves further study. Simulations with multiple AGN cycles should also be explored.

The model employed in this work for tracing the CRe was very simple—a tracer which was advected along with the fluid, initially set to unity for the material ejected by the jet or within the initial bubble. A more accurate model would treat the physics of the CRe explicitly, allowing for (re)acceleration by shocks and/or turbulence, cooling from radiative losses and Coulomb collisions, and/or diffusion and streaming (as in [ZuHone et al. 2013](#); [Donnert & Brunetti 2014](#); [ZuHone et al. 2015](#); [Yang & Ruszkowski 2017](#); [Winner et al. 2019](#); [Ogrodnik et al. 2020](#); [Domínguez-Fernández et al. 2020](#)). This would provide a way to more definitively determine if the energetic properties of the CRe can produce radio emission with a brightness and spectrum consistent with what is seen in observations, depending on the shock strength and local magnetic field.

With such a model for the energetics of the CRe, two obvious follow-ups to this work suggest themselves. First, a cluster with the spread-out CRe as presented in this work could undergo another merger, allowing the CRe to be passed over by a merger shock, providing an opportunity to see how the ICM and CRe physics interplay to produce relics with characteristic sizes, shapes, and brightnesses. Alternatively, a radio galaxy far from the cluster center could be included in a merger simulation, where the CRe from the galaxy’s radio lobes would be mixed into the local ICM by gas motions, and then reaccelerated by the merger shock as it passes by,

as in the scenario postulated by Shimwell et al. (2015).<sup>1</sup> These issues are beyond the scope of this initial exploratory work.

## ACKNOWLEDGMENTS

JAZ and PN acknowledge support from the Chandra X-ray Center, which is operated by the Smithsonian Astrophysical Observatory for and on behalf of NASA under contract NAS8-03060.

*Facilities:* Pleiades (NASA/Ames Research Center), Hydra (Smithsonian Institution)

*Software:* AstroPy<sup>2</sup> (Astropy Collaboration et al. 2013), Matplotlib<sup>3</sup> (Hunter 2007), NumPy<sup>4</sup>, yt<sup>5</sup> (Turk et al. 2011)

## REFERENCES

Ascasibar, Y., & Markevitch, M. 2006, ApJ, 650, 102

Astropy Collaboration, Robitaille, T. P., Tollerud, E. J., et al. 2013, A&A, 558, A33

Brunetti, G., & Lazarian, A. 2007, MNRAS, 378, 245

Brunetti, G. & Jones, T. W. 2014, International Journal of Modern Physics D, 23, 1430007-98

Brzycki, B., & ZuHone, J. 2019, ApJ, 883, 118

Colella, P., & Woodward, P. R. 1984, Journal of Computational Physics, 54, 174

Domínguez-Fernández, P., Brüggen, M., Vazza, F., et al. 2020, MNRAS. doi:10.1093/mnras/staa3018

Donnert, J. & Brunetti, G. 2014, MNRAS, 443, 3564. doi:10.1093/mnras/stu1417

Dubey, A., et al. 2009, Parallel Comput., 35, 512

Eddington, A. S. 1916, MNRAS, 76, 572

Ensslin, T. A., Biermann, P. L., Klein, U., et al. 1998, A&A, 332, 395

Enßlin, T. A. & Gopal-Krishna 2001, A&A, 366, 26

Evans, C. R., & Hawley, J. F. 1988, ApJ, 332, 659

Ferrari, C., Govoni, F., Schindler, S., et al. 2008, SSRv, 134, 93

Finoguenov, A., Sarazin, C. L., Nakazawa, K., et al. 2010, ApJ, 715, 1143

Giacintucci, S., Venturi, T., Macario, G., et al. 2008, A&A, 486, 347

Hernquist, L. 1990, ApJ, 356, 359

Hoang, D. N., Shimwell, T. W., Stroe, A., et al. 2017, MNRAS, 471, 1107

Hunter, J. D. 2007, Computing in Science and Engineering, 9, 90.

Kang, H., & Ryu, D. 2016, ApJ, 823, 13

Kazantzidis, S., Magorrian, J., & Moore, B. 2004, ApJ, 601, 37.

Kempner, J. C., Blanton, E. L., Clarke, T. E., et al. 2004, The Riddle of Cooling Flows in Galaxies and Clusters of Galaxies, 335

Lee, D., & Deane, A. E. 2009, Journal of Computational Physics, 228, 952

Macario, G., Markevitch, M., Giacintucci, S., et al. 2011, ApJ, 728, 82

Marinacci, F., Vogelsberger, M., Pakmor, R., et al. 2018, MNRAS, 480, 5113

Markevitch, M., Govoni, F., Brunetti, G., et al. 2005, ApJ, 627, 733

Markevitch, M., et al. 2020, in preparation

Mazzotta, P. & Giacintucci, S. 2008, ApJL, 675, L9. doi:10.1086/529433

Navarro, J. F., Frenk, C. S., & White, S. D. M. 1997, ApJ, 490, 493

Nolting, C., Jones, T. W., O'Neill, B. J., et al. 2019, ApJ, 876, 154. doi:10.3847/1538-4357/ab16d6

Nolting, C., Jones, T. W., O'Neill, B. J., et al. 2019, ApJ, 885, 80. doi:10.3847/1538-4357/ab4650

Ogreal, G. A., Brüggen, M., Röttgering, H., et al. 2013, MNRAS, 429, 2617

Ogreal, G. A., Brüggen, M., van Weeren, R., et al. 2014, MNRAS, 440, 3416

Ogrodnik, M., Hanasz, M., & Wóltański, D. 2020, arXiv:2009.06941

Pakmor, R., & Springel, V. 2013, MNRAS, 432, 176

<sup>1</sup> This is a distinct situation from the direct acceleration of plasma in radio lobes *before* it has mixed in with the ICM, as simulated recently by Nolting et al. (2019a,b)

<sup>2</sup> <http://www.astropy.org>

<sup>3</sup> <http://matplotlib.org>

<sup>4</sup> <http://www.numpy.org>

<sup>5</sup> <http://yt-project.org>

Roediger, E. & ZuHone, J. A. 2012, MNRAS, 419, 1338. doi:10.1111/j.1365-2966.2011.19794.x

Sanders, J. S., Fabian, A. C., Russell, H. R., et al. 2016, MNRAS, 460, 1898. doi:10.1093/mnras/stw1119

Sarazin, C. L. 1999, ApJ, 520, 529

Shimwell, T. W., Brown, S., Feain, I. J., et al. 2014, MNRAS, 440, 2901

Shimwell, T. W., Markevitch, M., Brown, S., et al. 2015, MNRAS, 449, 1486

Springel, V. 2010, MNRAS, 401, 791.

Turk, M. J., Smith, B. D., Oishi, J. S., Skory, S., Skillman, S. W., Abel, T., & Norman, M. L. 2011, ApJS, 192, 9

van Weeren, R. J., Röttgering, H. J. A., Brüggen, M., et al. 2010, Science, 330, 347

van Weeren, R. J., Brüggen, M., Röttgering, H. J. A., et al. 2011, MNRAS, 418, 230

van Weeren, R. J., Andrade-Santos, F., Dawson, W. A., et al. 2017, Nature Astronomy, 1, 0005

van Weeren, R. J., de Gasperin, F., Akamatsu, H., et al. 2019, SSRv, 215, 16

Vikhlinin, A., Markevitch, M., Murray, S. S., Jones, C., Forman, W., & Van Speybroeck, L. 2005, ApJ, 628, 655

Walker, S. A., Sanders, J. S., & Fabian, A. C. 2016, MNRAS, 461, 684. doi:10.1093/mnras/stw1367

Weinberger, R., Ehlert, K., Pfrommer, C., et al. 2017, MNRAS, 470, 4530

Winner, G., Pfrommer, C., Girichidis, P., et al. 2019, MNRAS, 488, 2235. doi:10.1093/mnras/stz1792

Yang, H.-Y. K. & Ruszkowski, M. 2017, ApJ, 850, 2. doi:10.3847/1538-4357/aa9434

ZuHone, J. A., Markevitch, M., & Johnson, R. E. 2010, ApJ, 717, 908

ZuHone, J. A., Markevitch, M., & Lee, D. 2011, ApJ, 743, 16

ZuHone, J. A., Markevitch, M., Brunetti, G., & Giacintucci, S. 2013, ApJ, 762, 78

ZuHone, J. A., Brunetti, G., Giacintucci, S., et al. 2015, ApJ, 801, 146. doi:10.1088/0004-637X/801/2/146

ZuHone, J. A., Miller, E. D., Simionescu, A., & Bautz, M. W. 2016, ApJ, 821, 6

ZuHone, J. A., Miller, E. D., Bulbul, E., et al. 2018, ApJ, 853, 180

ZuHone, J. A., Zavala, J., & Vogelsberger, M. 2019, ApJ, 882, 119